

Radial matrix constraint influences tissue contraction and promotes maturation of bi-layered skin equivalents

Jessica Polak^{a,*}, David Sachs^a, Nino Scherrer^b, Adrian Süess^a, Huan Liu^c, Mitchell Levesque^e, Sabine Werner^c, Edoardo Mazza^{a,d}, Gaetana Restivo^e, Mirko Meboldt^a, Costanza Giampietro^{a,d}

^a Department of Mechanical and Process Engineering, ETH Zurich, Zurich 8092, Switzerland

^b Department of Computer Science, ETH Zurich, Zurich 8092, Switzerland

^c Institute of Molecular Health Sciences, Department of Biology, ETH Zurich, Zurich 8093, Switzerland

^d Swiss Federal Laboratories for Materials Science and Technology (EMPA), Dübendorf 8600, Switzerland

^e Department of Dermatology, University Hospital Zurich, Zurich 8091, Switzerland

ARTICLE INFO

Keywords:

Radial matrix constraint
In vitro human skin equivalent
Collagen hydrogel
3D-printed culture system
Tissue organization
Keratinocyte differentiation
Extracellular matrix production
Mechanical stimulus
Finite element simulation

ABSTRACT

Human skin equivalents (HSEs) serve as important tools for mechanistic studies with human skin cells, drug discovery, pre-clinical applications in the field of tissue engineering and for skin transplantation on skin defects. Besides the cellular and extracellular matrix (ECM) components used for HSEs, physical constraints applied on the scaffold during HSEs maturation influence tissue organization, functionality, and homogeneity.

In this study, we introduce a 3D-printed culture insert that exposes bi-layered HSEs to a static radial constraint through matrix adhesion. We examine the effect of various diameters of the ring-shaped culture insert on the HSE's characteristics and compare them to state-of-the-art unconstrained and planar constrained HSEs.

We show that radial matrix constraint of HSEs regulates tissue contraction, promotes fibroblast and matrix organization that is similar to human skin in vivo and improves keratinocyte differentiation, epidermal stratification, and basement membrane formation depending on the culture insert diameter.

Together, these data demonstrate that the degree of HSE's contraction is an important design consideration in skin tissue engineering. Therefore, this study can help to mimic various in vivo skin conditions and to increase the control of relevant tissue properties.

1. Introduction

Human skin equivalents (HSEs) are highly relevant in vitro culture systems to investigate fundamental cellular behavior and functions of the skin. Reconstituted from cells and extracellular matrix (ECM) components, HSEs are used to mimic native tissue with the aim to uncover biological processes in health and disease conditions, and to develop novel treatment options or tissue replacements [1–3]. Many biological processes (e.g., growth, remodeling) and in vivo skin conditions are characterized by different structural and functional properties [4–6]. Besides the integration of donor-specific cells in HSEs, such properties can be modulated through matrix interventions, including changing the matrix protein concentration [7–9], alterations in chemical cross-linking [10], changing polymerization conditions [11] or through applying external mechanical loadings [12–15]. As cells are embedded within the matrix, such interventions not only affect the matrix properties but also

indirectly affect cellular morphology and behavior [16]. The cells in response remodel the matrix, resulting in a complex feedback system [17–24]. While all these techniques allow modulating the properties of the matrix, applying external mechanical constraints to HSEs enable a modulation without affecting the initial biochemical composition of the matrix.

To expose HSEs to mechanical stress and strain, cell-populated single-protein matrices (e.g. collagen type I or fibrin) are commonly anchored or glued to rigid support structures using adhesion or pinching techniques [25–27]. In contrast, commonly cultured free-floating tissue constructs are free of external mechanical stresses [28]. As an alternative, early studies have employed a tissue construct whose matrix is planarly restrained at the bottom through membrane adhesion. While free-floating tissue models contracted to a minimal size with tissue of low cell-matrix tension, the planarly restrained tissue models resulted in tissue of higher cell-matrix tension and different morphological

* Corresponding author: Department of Mechanical and Process Engineering, ETH Zurich, 8092 Zurich, Switzerland.

E-mail address: jessica.polak@gmail.com (J. Polak).

<https://doi.org/10.1016/j.bioadv.2023.213702>

Received 10 May 2023; Received in revised form 26 October 2023; Accepted 12 November 2023

Available online 14 November 2023

2772-9508/© 2023 The Authors. Published by Elsevier B.V. This is an open access article under the CC BY license (<http://creativecommons.org/licenses/by/4.0/>).

structure [29–33]. Further studies have shown an interdependence of mechanical matrix constraints and cellular functions [34]. These findings have sparked the development of a variety of approaches that expose HSEs to different static or dynamic mechanical cues. These approaches vary significantly in their applied anchoring techniques and geometries, as well as in the applied mechanical stimuli (see Supplementary F for a detailed overview and classification of existing approaches along various design axes). In the simplest form, static physical constraints expose tissue constructs to an external static stress and hence limit the degrees of freedom of tissue deformation [15,26,27,35]. The magnitude of the resulting stress depends on the geometry of the anchoring structure [36,37], its material properties [38] or on the magnitude of the externally applied force that results in an additional static elongation of the tissue [38–40]. However, only a few studies investigate the effect of varying constraint magnitudes [38–40]. While John et al. (2010) and Derderian et al. (2005) have studied the effect of multiple levels of bi-axial constraint in dermal-only HSEs, Powell et al. (2010) have studied the effect on bi-layered HSEs under multiple levels of uniaxial stretch.

In this work, we investigate the effect of various levels of radial constraints on the characteristics of bi-layered, collagen-based HSEs. Therefore, we developed a 3D-printed, ring-shaped culture insert that enables the adhesion of HSEs via its hydrophilic surface. Varying the diameter of the ring-shaped culture insert allows us to expose the HSE to distinct levels of radial area constraints. We compare three levels of radially constrained (RC) HSEs to state-of-the-art unconstrained free-floating (FF), and planar constrained (PC) HSEs. Our experimental results demonstrate that solely varying the diameter of the culture insert leads to significant changes in the HSE's organization, maturation, and homogeneity. In fact, dermal organization, epidermal stratification, and

basement membrane formation positively correlate with the culture insert diameter. Our findings have important implications on the design of collagen-based HSEs and can help to increase the reproducibility of HSE fabrication.

2. Materials and methods

2.1. Design and fabrication of a novel culture system for peripheral attachment of HSEs

We developed a culture system that allows guiding the magnitude of radial contraction of HSEs during culturing. To achieve this goal, we introduced a hydrophilic culture insert that enables a minimally-invasive peripheral hydrogel attachment. The system is fully customizable and can be adapted to any culture plate. It consists of two parts, the culture insert (Fig. 1a) and the insert holder (Fig. 1b). The culture insert is composed of a lower ring for hydrogel attachment, an upper ring for stabilization, as well as three hangers with anchoring knobs that enable a fixed position of the culture insert in a commercially available transwell insert (culture area: 113 mm²; Corning) and in the custom designed insert holder (Fig. 1c). By varying the diameter of the lower ring, the effect of the boundary conditions on the HSE can be varied. Culture inserts were produced in three different sizes: Small (S): 11.3 mm²; Medium (M): 33.9 mm²; Large (L): 67.8 mm² (Supplementary A, A). The insert holder (Supplementary A, B) is compatible with commercially available deepwell plates (Fig. 1c) and enables convenient medium change as well as culture of the HSE at the air-liquid interface (ALI) (Fig. 1d). All parts of the culture system were designed with a commercial computer-aided design (CAD) software (Autodesk Fusion 360) and fabricated with a 3D-printer (XFAB 2000, DWS Systems) using

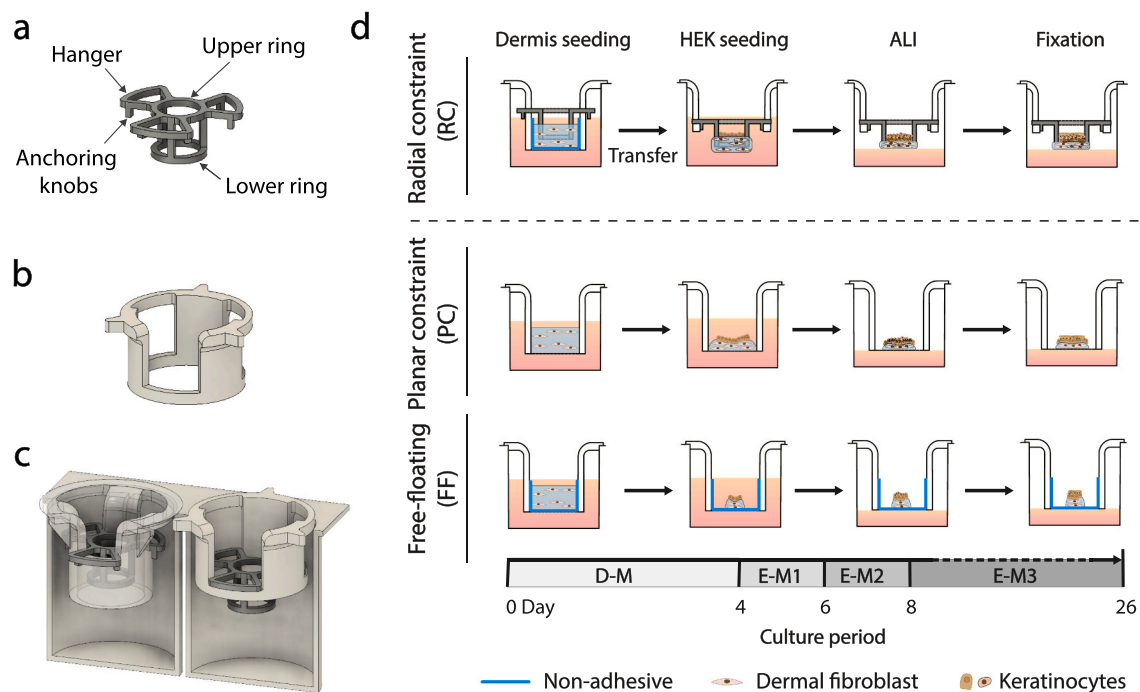


Fig. 1. Schematics of the culture system and overview of the human skin equivalent (HSE) fabrication process.

(a) The culture insert was designed for peripheral attachment of the HSE at the lower ring. (b) The insert holder enables easy medium change and culture of the HSE at the air-liquid interface. (c) The upper ring and the three hangers with anchoring knobs ensure a fixed position of the culture insert within a commercially available transwell insert (left) and the insert holder (right) during dermis seeding and culture, respectively. (d) Schematics and timeline of the HSE fabrication process. Transwell inserts were treated to be non-adhesive for radially constrained (RC) and free-floating (FF) conditions. The dermal equivalent was produced by mixing primary human dermal fibroblasts (HDFs) with collagen type I and cultured in Dermis-Medium (D-M). The 3D-printed culture insert was transferred to the insert holder in RC conditions before seeding of human epidermal keratinocytes (HEKs). HEKs were seeded on top of the dermal layer on day 4 and cultured in Epidermis-Medium 1 (E-M1). Two days later, HSEs were cultured in Epidermis-Medium 2 (E-M2). HSEs were lifted and incubated at the air-liquid interface (ALI) on day 8 and cultured in Epidermis-Medium 3 (E-M3) for further 18 days until fixation.

the acrylic polymer Vitra 413 (DWS Systems). Printed culture inserts and holders were coated with 10 µm parylene C using Parylene P6 coater (Diener) for a defined and biocompatible surface. The coated products were sterilized by autoclaving at 120 °C. The sterilized culture inserts were activated with oxygen plasma at 100 W for 1 min directly before usage to increase the surface hydrophilicity.

2.2. Cell isolation and cell culture

Primary HDFs and HEKs were isolated from adult abdominal healthy skin. Native human skin biopsies were provided by the plastic surgery department of the University Hospital Zurich with the assistance of the SKINTEGRITY.CH biobank. All samples used were surplus materials from routine surgeries. Informed consent had been obtained from all patients, and all experiments were conducted according to the principles set out in the WMA Declaration of Helsinki and the Department of Health and Human Services Belmont Report. The use of material for research purposes had been approved by the local ethic commission (KEK Nr. 2017-00688).

Biopsies were stored before use in Hank's balanced salt solution (HBSS, Gibco) supplemented with gentamycin (5 µg/ml, Gibco). Cell isolation and culture of HDFs and HEKs were adapted from a previously published protocol [41]. Skin pieces were incubated in 9 U/ml dispase II (10 mg/ml, Roche, Cat. No. Roche 04942078001), HBSS and gentamycin (5 µg/ml, Gibco) at 4 °C overnight. The day after, the epidermis was peeled off from the dermis.

The epidermis was digested in 0.1 % trypsin (Gibco), 0.02 % EDTA (Sigma) in phosphate-buffered saline without Mg^{2+} and Ca^{2+} (PBS⁻, Gibco) for 5 min at 37°, before carefully pipetting up and down. Digestion was stopped by adding HBSS, and the suspension was filtered through a cell strainer (70 µm, Corning) and centrifuged at 1200 rpm and 4 °C for 5 min. HEKs were resuspended in keratinocyte medium (800'000 cells/60 cm², Gibco) and cultured at 37 °C and 5 % CO₂. Culture medium was exchanged every other day. HEKs were splitted at a confluency of max 70 %.

The dermis was minced in small pieces and incubated in collagenase (1 mg/ml, Sigma), 0.5 mM CaCl₂ in PBS⁻ for 2 h at 37 °C. Following vortexing every 20 min, the cell suspension was filtered with a cell strainer (70 µm, Corning) and centrifuged at 1200 rpm for 5 min. The cell pellet was resuspended and cultured in Dulbecco's Modified Eagle Medium (DMEM, Gibco) supplemented with 5 % heat-inactivated fetal bovine serum (FBS, Gibco) and 1 % antibiotics (penicillin-streptomycin, Sigma) at 37 °C, 5 % CO₂. The day after, fibroblasts were washed with PBS⁻ before medium was changed. HDFs were splitted when they reached 80 % confluency. From thereon, medium was changed every other day.

2.3. Production and cultivation of HSEs

HSEs exhibiting static radial constraint (RC) were produced in three different sizes (RC-S, RC-M, RC-L). Unconstrained (free-floating, FF) and membrane-restrained (planar constraint, PC) HSEs were produced to represent state-of-the-art HSEs. For the contraction assay, equivalents without cells were produced additionally and served as negative control. The production of collagen-based HSEs was modified from a previously published protocol [42] and is shown in Fig. 1d. First, transwell inserts with a 0.4 µm polycarbonate membrane (culture area: 113 mm²; Corning) were coated with 5 % BSA (Sigma) in PBS⁻ for 30 min @ 37 °C to prevent hydrogel adherence in RC and FF conditions. 3D-printed inserts were placed into the transwell for the RC groups. A neutralization buffer was prepared by supplementing DMEM with 30 % FBS, 3 % glutamine (200 mM), 3 % penicillin-streptomycin and 15 % sodium bicarbonate (7.5 %). Bovine collagen type I (5 mg/ml, Gibco) was diluted to 3 mg/ml with PBS⁻. Cultured HDFs were harvested at passage 6 and resuspended at a concentration of 4.3 mio cells/ml in DMEM supplemented with 10 % FBS and 1 % penicillin-streptomycin. All

components were kept on ice before mixing. For a final volume of 4.65 ml (enough for 6 HSEs), 350 µl of the cell suspension were subsequently mixed with 1.12 ml of the neutralization buffer and 3.18 ml type I collagen (3 mg/ml). Per dermal equivalent, 750 µl of the solution with 250'000 human dermal fibroblasts was seeded. After a 10 min incubation at room temperature (RT), dermal equivalents were kept in an incubator at 37 °C for 1 h to allow polymerization. Dermal equivalents were cultured in Dermis-Medium (D-M); DMEM supplemented with 10 % FBS, ascorbic acid (200 µg/ml, Sigma) and 1 % antibiotics for 3 days before HEK seeding. On day 4, inserts were removed in the RC HSEs and transferred from the transwell insert to the holder to allow easy medium change. The control groups (PC and FF) were kept in the transwell inserts. Dermal equivalents were incubated at 37 °C for 1 h in HBSS. Cultured HEKs were harvested at passage 2 and resuspended in DMEM at a cell suspension of 30'000'000 cells/ml and kept at RT for 10 min. HBSS was removed from the dermal equivalents, and 10 µl of the keratinocyte suspension was seeded in the center on top of the dermal equivalent in one droplet. HSEs were incubated for 45 min at 37 °C before cultured in Epidermis-Medium 1 (E-M1); 3 parts DMEM, 1 part HAM'S F12 Nutrient Mix (Gibco), 0.4 µg/ml hydrocortisone (Sigma-Aldrich), 5 µl/ml ITES (Insulin-Transferrin-Selenium-Ethanolamine 100×, Gibco), 0.1 mM O-phosphorylethanolamine (Sigma-Aldrich), 0.18 mM adenine hydrochloride hydrate (Sigma-Aldrich), 0.004 nM progesterone (Sigma-Aldrich), 2.4 mM calcium chloride dihydrate (Sigma-Aldrich), 0.02 nM triiodo-L-thyronine sodium salt (Sigma-Aldrich), 0.1 % chelexed newborn calf serum (Gibco), 200 µg/ml ascorbic acid and 1 % penicillin-streptomycin. Two days later, HSEs were incubated in Epidermis-Medium 2 (E-M2); 3 parts DMEM, 1 part HAM'S F12 Nutrient Mix, 0.4 µg/ml hydrocortisone, 5 µl/ml ITES, 0.1 mM O-phosphorylethanolamine, 0.18 mM adenine hydrochloride hydrate, 0.004 nM progesterone, 2.4 mM calcium chloride dihydrate, 0.02 nM triiodo-L-thyronine sodium salt, 0.1 % non-chelexed newborn calf serum, 200 µg/ml ascorbic acid and 1 % penicillin-streptomycin. Two days later, HSEs were lifted to the air-liquid interface (ALI) and cultured for 18 days in Epidermis-Medium 3 (E-M3); 1 parts DMEM, 1 part HAM'S F12 Nutrient Mix, 0.4 µg/ml hydrocortisone, 5 µl/ml ITES, 0.18 mM adenine hydrochloride hydrate, 2.4 mM calcium chloride dihydrate, 0.02 nM triiodo-L-thyronine sodium salt, 2 % non-chelexed newborn calf serum, 200 µg/ml ascorbic acid and 1 % penicillin-streptomycin. Medium was changed every other day.

2.4. Finite element simulation

The FEM analysis was conducted using a custom written code in COMSOL Multiphysics® 6.0 (COMSOL Multiphysics®, COMSOL AB, Stockholm, Sweden). The material parameters used for all finite element simulations are reported in Supplementary D, Table 3. The hydrogel was modelled using the framework of porous media mechanics [43,44]. To account for the specific nature of the collagen hydrogels, the model accounts (1) for the spontaneous contraction of the gel independent of the cells and (2) for the contraction induced by the presence of the fibroblasts. To account for the spontaneous contraction, we split the deformation gradient F into a passive mechanical contribution F_{pm} and a contraction F_c [45]

$$F = F_{pm} F_c. \quad (1)$$

Therein F_c represents the spontaneous contraction, which is assumed isotropic. It is prescribed by

$$F_c = \begin{pmatrix} \lambda_c & 0 & 0 \\ 0 & \lambda_c & 0 \\ 0 & 0 & \lambda_c \end{pmatrix}, \quad (2)$$

with $\lambda_c = 0.8$. The passive mechanical contribution of the gel is modelled as a biphasic porous medium consisting of a solid and a liquid phase. Assuming quasi-static conditions, the absence of body forces and

incompressibility of each phase, the conservation of mass and momentum read [46,47]

$$\text{div}(\mathbf{v}_s + \mathbf{q}) = 0, \quad (3a)$$

$$\text{div}(\boldsymbol{\sigma}) = 0. \quad (3b)$$

Therein \mathbf{v}_s denotes the spatial velocity of the solid, \mathbf{q} the flow of the liquid, and $\boldsymbol{\sigma}$ the Cauchy stress tensor of the mixture. To introduce the active contraction of the cells, an additional term $\boldsymbol{\sigma}_a$ is considered in the stress tensor. The total stress then reads

$$\boldsymbol{\sigma} = \boldsymbol{\sigma}_{pm} - p\mathbf{I} + \boldsymbol{\sigma}_a. \quad (4)$$

Therein $\boldsymbol{\sigma}_{pm}$ results from the passive mechanical deformation of the chosen strain energy function, p is the hydrostatic pressure of the liquid phase and $\boldsymbol{\sigma}_a$ is the active contribution of the fibroblasts. The latter is assumed isotropic and modelled as

$$\boldsymbol{\sigma}_a = \begin{pmatrix} \sigma_0 & 0 & 0 \\ 0 & \sigma_0 & 0 \\ 0 & 0 & \sigma_0 \end{pmatrix}. \quad (5)$$

The fibroblast stress $\sigma_0 = 4.5$ kPa was chosen according to values in the literature [48]. The elastic contribution to the stress is modelled using a Rubin-Bodner model [49]. The values for the material parameters of the Rubin-Bodner model are reported in Supplementary Table 3. For a detailed description of the model, the reader is referred to the literature [50,51]. Osmotic effects have been neglected in the present implementation. The model parameters are selected based on experimental data from literature [52]. The simulation starts from the initial zero energy configuration. In a first step the spontaneous contraction is applied and in a second step the force of the fibroblasts is activated. The simulation runs until a new equilibrium is reached. The finite element models are shown in Supplementary Fig. 1.

2.5. Hematoxylin and eosin staining (H&E)

For histological analysis, samples were fixed in 4 % paraformaldehyde for 2 h at RT and embedded in Tissue-Tek O.C.T. compound (Sakura). H&E-staining was performed on sections of 10 μm following the instructions of the staining kit manufacturer (Biosystems). The stained sections were imaged with a digital scanner (Pannoramic 250, 3DHistech).

2.6. Immunofluorescence staining

For immunofluorescence staining, samples were fixed in 4 % paraformaldehyde for 2 h at RT and embedded in Tissue-Tek O.C.T. and frozen. Sections of 10 μm thickness were dried for 5 min at RT and subsequently washed in PBS. Samples were permeabilized twice with PBS/0.1 % Triton X-100 for 5 min at RT. After washing twice with PBS for 5 min, sections were incubated with 5 % BSA in PBS/0.1 % Tween 20 for 1 h at RT. Primary antibody was applied overnight at 4 °C. The next day, sections were washed twice in PBS/0.1 % Triton X-100 for 10 min at RT and once in PBS for 5 min. Secondary antibody and DAPI were incubated for 1 h at RT. Sections were washed twice in PBS/0.1 % Triton X-100 for 5 min, once in PBS for 5 min before mounting with fluoroshield histology mounting medium (Sigma, F6182). Details of primary and secondary antibodies are included in Supplementary Table 1. All fluorescence microscopy images were captured with an inverse confocal laser scanning microscope (Leica SP8) or with a digital scanner (Pannoramic 250, 3DHistech). For comparison purposes, different sample images of the same antigen were acquired under constant acquisition settings.

2.7. Quantitative analysis

2.7.1. Contraction assay

Macroscopic images were acquired every day during HSE culture with an USB microscope (Toolcraft) and the MicroCapture Plus v3.1 software (ProScope). To quantify the global radial contraction, the area of each HSE was measured at each timepoint with ImageJ (National Institutes of Health, Bethesda, MD). The radial contraction at timepoint t is defined as the area at the timepoint t (A_t) divided by the initial area of each HSE (A_0) after polymerization.

2.7.2. Layer thickness measurements

Epidermal, dermal, and total thickness were measured in sections stained with H&E (10 μm). For every sample, at least 3 sections in different depths were analyzed. For each section, at least 3 measurements were obtained. Measurements were performed using the QuPath software [53].

2.7.3. Determination of basal keratinocytes per length epidermal equivalent

To obtain the relative quantity of basal keratinocytes per length, the basal area was first manually segmented. In a further step, cells were detected and counted using QuPath [53]. Finally, the number of cells was normalized by length measurements that were obtained using QuPath.

2.7.4. Epidermal and dermal cell proliferation

The proliferation rate of cells was quantified by counting Ki67-positive nuclei in the dermis, or in the basal or low suprabasal epidermis using QuPath [53]. For every sample, at least 3 sections in different depths were analyzed.

2.7.5. Directionality and alignment analysis

To quantify the directional properties of cell nuclei and fibers, a custom-made cross-platform script was developed. The script requires the definition of regions of interests (ROIs) and tissue labels (e.g., dermis, epidermis) in QuPath [53]. Based on the assigned labels, the script automatically exports relevant parts from QuPath and processes them in Fiji. The in-plane orientation of vimentin-stained fibroblasts, fibroblast nuclei and dermal ECM was computed using the OrientationJ plug-in for ImageJ (National Institutes of Health, Bethesda, MD) over three images for each condition. To compare the orientational distribution across conditions, we aligned the dominant in-plane orientation per condition to an angle of 0°. The custom-made scripts will be made available upon request.

2.8. qRT-PCR

To separate epidermal from dermal equivalents, HSEs were incubated in dispase (0.9 U/ml, Roche) for 30 min at 37 °C. The epidermal equivalent was removed from the dermal equivalent by forceps. Epidermal and dermal equivalent were snap-frozen in Trizol immediately after collection and stored at −80 °C until RNA isolation. Samples were homogenized with a TissueLyser II (Qiagen) for 3 min at 30 Hz. RNA was isolated using phenol/chloroform extraction according to the manufacturer's protocol (Trizol™ Reagent, Invitrogen). To generate cDNA, RNA was reverse transcribed using Reverse Transcription System (Promega). qRT-PCR was performed in triplicates on an Applied Biosystems ViiA 7 system (Thermo Fisher Scientific) using Fast SYBR™ Green Master Mix (4385612, Applied Biosystems™). The expression level of each target gene was normalized to expression levels of the *RPL27* housekeeping gene. Fold change was normalized to the control group (PC). The primers for qRT-PCR are listed in Supplementary Table 2.

2.9. Statistics and reproducibility

Statistical analysis was performed using GraphPad Prism 9. Datasets were first tested for normal distribution using the Shapiro–Wilk test. All data showing normal distribution were analyzed using a parametric test, i.e. one-way ANOVA followed by Turkey's multiple comparison test. Non-parametric data were analyzed using Kruskal–Wallis's tests followed by Dunn's multiple comparison test. For each plot, the statistical test applied is specified in the corresponding legend. Analysis of samples was performed at least in triplicate and averaged. The difference between groups was regarded significant at $P < 0.05$. All analyses report mean \pm standard deviation (SD). SD is shown using error bars for bar plots and error bands for line plots.

3. Results

3.1. Radial constraint in HSEs influences macroscopic appearance and tissue contraction

3.1.1. Macroscopic morphology of HSEs

We first analyzed the morphological appearance of HSEs after 26 days of culture. Representative macroscopic images (upper panel) and H&E-stained cross-sectional views (lower panel) of the HSEs are shown in Fig. 2a. Overall, all HSEs showed a bi-layered structure composed of a dermal equivalent (pink) covered by a stratified epidermal equivalent (purple).

Cell-mediated collagen contraction is a characteristic of 3D cultures [29]. Macroscopically, the planarly constrained (PC) and free-floating (FF) samples had a trapezoidal shape (Fig. 2a, H&E panel) due to the contraction of the less-constrained upper half of the HSEs. Moreover, free of external physical constraints, the FF-HSEs contracted to the expected convex spheroid of minimal size [28,29,32]. The RC-HSEs contracted to a slightly concave disk of the size of the corresponding lower ring, i.e., S, M and L. Across all conducted experiments, all RC-HSEs remained peripherally attached to the culture insert (indicated with an arrow in Fig. 2a) and did not contract further than the size of the lower ring of the corresponding culture insert, while within the PC samples, the dermal layer remained adherent on the membrane surface of the transwell insert for 3 out of 4 samples. The detached PC samples were excluded from further analysis. Overall, the radially constrained HSEs showed a characteristic macroscopic appearance (Fig. 2a). The epidermal (Fig. 2b) and dermal (Fig. 2c) thickness in the H&E cross-sections was measured, but no significant differences between the PC and FF samples were observed. As expected, within the RC-HSEs, the dermal thickness of the HSEs decreased with increasing culture insert diameter (Fig. 2c), while an opposite trend was observed for the epidermal thickness that significantly decreased in RC-S but increased to a similar extent in the RC-M and RC-L samples (Fig. 2b).

3.1.2. Global contraction of HSEs

A quantification of radial contraction over 26 days of the HSEs is shown in Fig. 2d. The radial contraction is defined as the area at

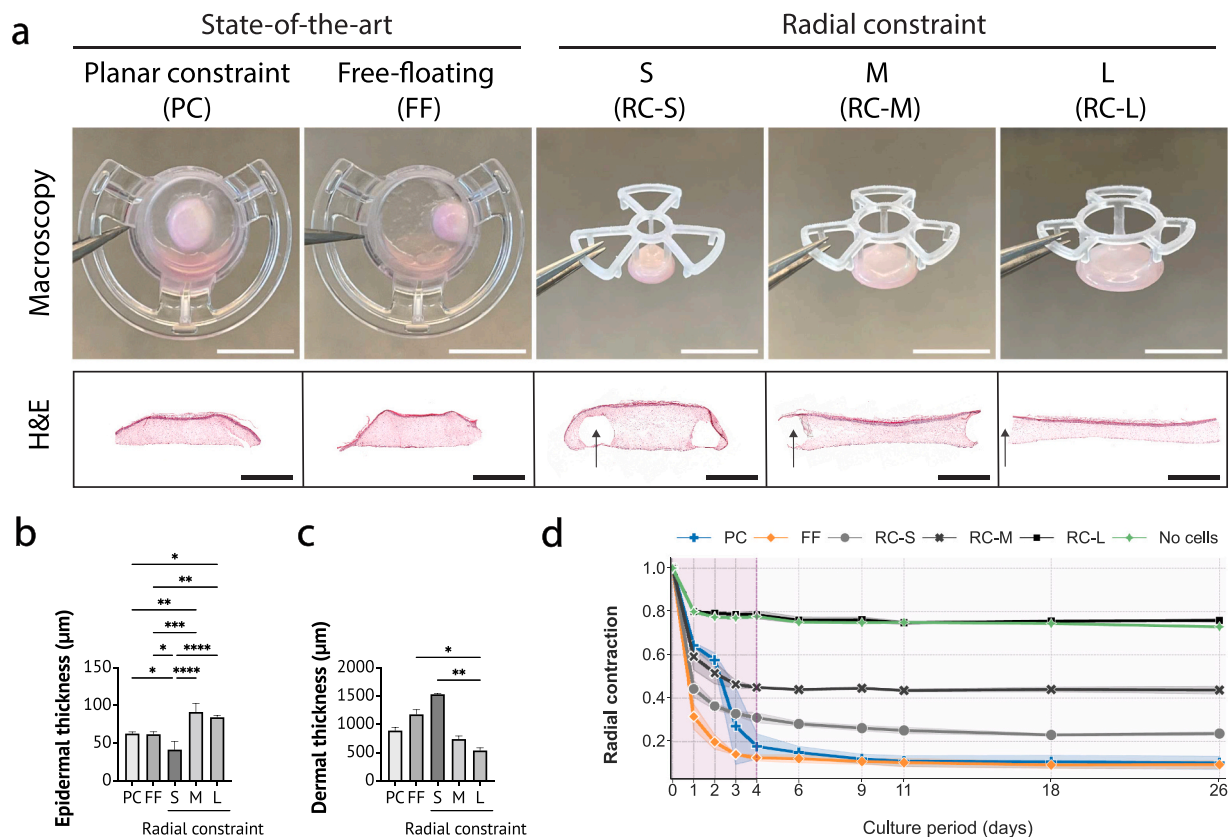


Fig. 2. Macroscopic analysis of HSEs shows an effect of radial constraint.

(a) Representative macroscopic images (upper panel) and hematoxylin & eosin (H&E)-stained cross-sections (lower panel) of HSEs from all experimental groups after 26 days of culture: Planar constraint (PC), free-floating (FF), radial constraint S (RC-S), radial constraint M (RC-M) and radial constraint L (RC-L). The depicted arrow points to the location of the 3D-printed culture insert. Scale bars; 10 mm for macroscopic images and 2 mm for H&E cross-sections.

(b) Epidermal thickness of the produced HSEs after 26 days of culture was measured in H&E-stained sections. $*P < 0.05$, $**P < 0.01$, $***P < 0.001$, $****P < 0.0001$ (one-way ANOVA with Turkey's multiple comparison test). (c) Dermal thickness of the produced HSEs after 26 days of culture was measured in H&E-stained sections. $*P < 0.05$ and $**P < 0.01$ (Kruskal–Wallis test with Dunn's multiple comparison test). (d) Radial area contraction of HSEs over the total culture period (26 days). Graphs show mean \pm standard deviation (SD; shadowed areas in (d) and error bars in the other graphs).

timepoint t (A_t) divided by the initial area of each HSE after polymerization (A_0). The observed behavior can be divided into two phases of contraction [54]. The greatest contraction rate was observed between day 1 and day 4 for all HSEs. From day 1 the area gradually decreased in the FF and RC samples, whereas the PC samples showed an irregular contraction behavior. The observed radial contraction of the RC-HSEs was limited by the size of the lower ring in the culture inserts which were chosen to be at 20 % (RC-S), 50 % (RC-M) and 80 % (RC-L) of the

initial area. Thereby, the RC-L sample was set as the maximal possible HSE area which was confirmed by the contraction of the no-cell control that radially contracted only minimally after day 3 and stabilized at approximately 80 % of the initial area. Overall, HSEs stopped to radially contract after day 6 of cultivation across all conditions and remained stable for the rest of the culturing phase.

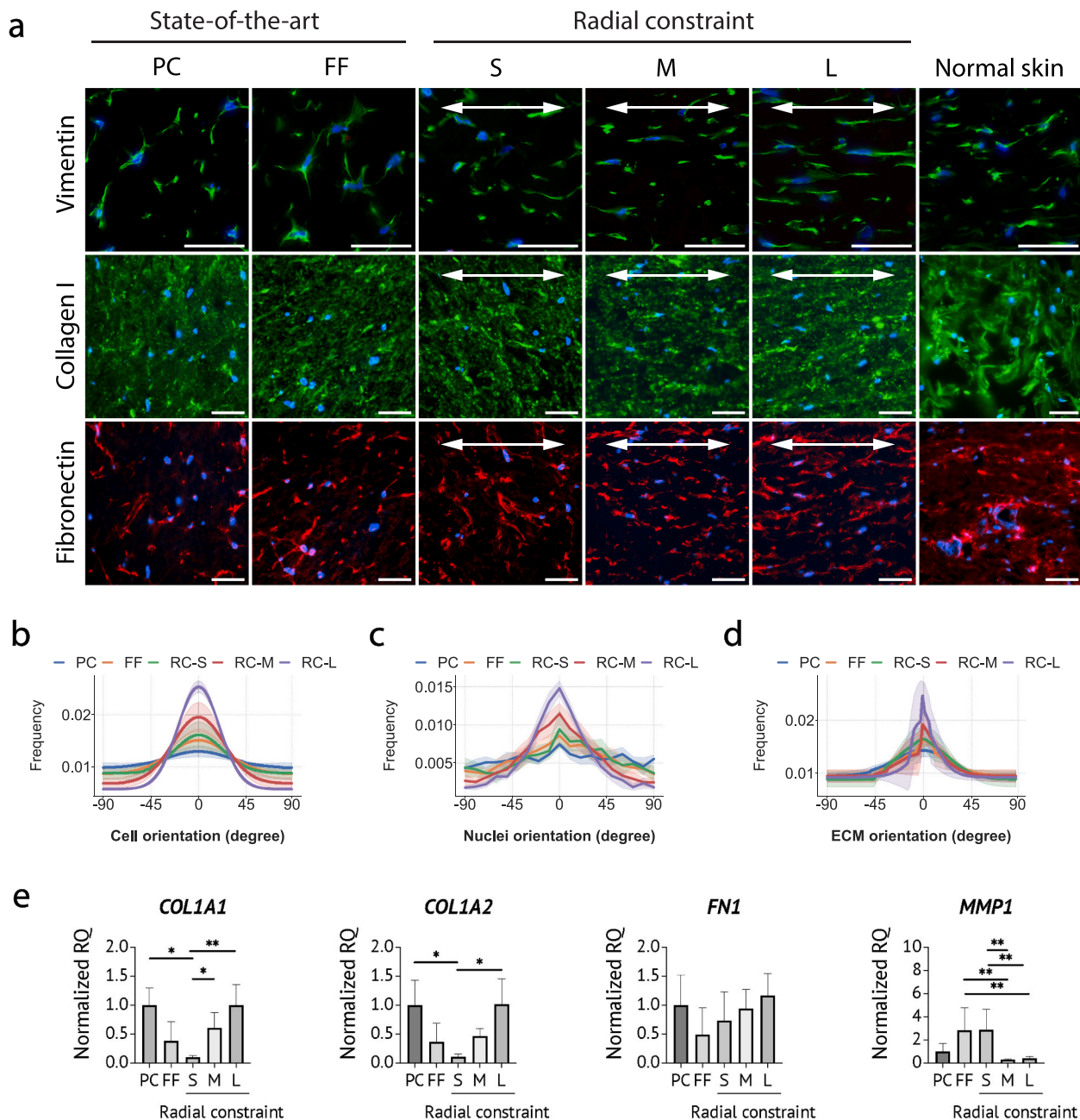


Fig. 3. Fibroblasts and matrix fibers in radially constrained HSEs are more aligned than in conventional HSEs.

(a) Representative immunofluorescence staining of sections from HSEs after 26 days of culture and of normal human skin for vimentin, collagen type I and fibronectin, and counterstaining of nuclei with DAPI. The depicted arrows indicate the direction of strain. Scale bars; 50 μ m **(b)** Cell in-plane orientation of vimentin-stained fibroblasts. The dominant in-plane orientation per condition is thereby aligned to an angle of 0°, whereas 90° is perpendicular to it. **(c)** In-plane orientation of fibroblast nuclei. The dominant in-plane orientation per condition is thereby aligned to an angle of 0°, whereas 90° is perpendicular to it. **(d)** In-plane orientation of dermal ECM (collagen I). The dominant in-plane orientation per condition is thereby aligned to an angle of 0°, whereas 90° is perpendicular to it. **(e)** qRT-PCR using RNA samples from different HSEs for *COL1A1*, *COL1A2*, *FN1* and *MMP1* relative to *RPL27*.

Graphs show mean \pm SD. * $P < 0.05$, ** $P < 0.01$ (one-way ANOVA with Turkey's multiple comparison test).

3.2. Analysis of the dermal equivalent

3.2.1. Static radial constraint affects fibroblast morphology and alignment in HSEs

Healthy or diseased native skin has a characteristic fibroblast morphology and collagen fiber orientation [55,56]. Mechanical loading influences dermal cell and ECM fiber alignment, gene expression and the overall maturation of HSEs [41,57,58]. Cross-sections of the samples were therefore immunostained with antibodies against vimentin and costained with DAPI to visualize fibroblast morphology and nuclei orientation within the dermis, respectively. As shown in Fig. 3a–c, in both PC and FF-HSEs, fibroblasts displayed a stellar shape with poor cell and nuclei alignment. In contrast, in all RC samples, fibroblasts showed a spindle shape morphology and were elongated and aligned with a prominent orientation in the direction of the strain forces applied. Of interest, higher culture insert diameter resulted in a more elongated fibroblast morphology and in a stronger orientational alignment of fibroblasts and nuclei. Qualitatively, native skin showed cell and nuclei alignment comparable to RC samples (Fig. 3a). We also quantified fibroblast density (Suppl. Fig. 2A), which inversely correlated with the thickness of the dermal equivalent (Fig. 2c). While the thickness of the dermal equivalent decreased with an increasing culture insert diameter, fibroblast density showed a positively correlated relationship with the culture insert diameter. No significant difference in fibroblast proliferation was detected as revealed by Ki67 staining (Suppl. Fig. 2B).

3.2.2. Static radial constraint regulates expression of ECM proteins and tissue orientation

We next analyzed the effect of differently sized culture insert diameter on the fiber alignment of the extracellular matrix (ECM) proteins collagen type I and fibronectin (Fig. 3a). In line with the effect on fibroblasts, we observed poor alignment of the fibers in PC and FF samples (Fig. 3d). In contrast, RC samples showed a prominent fiber direction that converged with increasing diameter to the main stress direction (Fig. 3d). Finally, we measured the relative expression of dermal ECM genes, including the genes encoding collagens $\alpha 1$ and $\alpha 2$ and fibronectin (*COL1A1*, *COL1A2*, *FN*), and expression of matrix metalloproteinase 1 (*MMP1*). We observed an increase in *COL1A1* and *COL1A2* expression in RC samples that was dependent on the culture insert diameter (Fig. 3e), while no significant differences in *FN* expression was observed. Interestingly, the RC-L samples showed similar expression levels for *COL1A1*, *COL1A2* and *FN* as the PC samples. Expression of *MMP1*, which encodes the major collagen degradation enzyme, was significantly downregulated in the PC and RC-M and RC-L [39]. We further measured the relative gene expression of the myofibroblast marker gene α smooth muscle actin (*ACTA2*). At the time point of fixation (day 26), the differences in *ACTA2* expression were not significant (Suppl. Fig. 2C, D), suggesting that radial constraint does not trigger pathological myofibroblast differentiation.

3.3. Analysis of the epidermal equivalent and of the basement membrane

3.3.1. Radial physical constraint of HSEs enhances stratification of keratinocytes

We next analyzed the effect of differently sized culture insert diameter on the structure of the dermal equivalent and on keratinocyte differentiation by H&E-staining (uppermost panel), immunofluorescence staining, and qRT-PCR analysis (Fig. 4). The H&E-stained sections (Fig. 4a) showed the characteristic layers of the stratified epidermis in all HSEs and in normal skin. Across all produced HSEs, we observed a basal layer (*stratum basale*) with cuboidal-shaped keratinocytes, a spinous layer (*stratum spinosum*) with circular-shaped keratinocytes, as well as granular and cornified layers (*stratum granulosum* and *stratum corneum*). In comparison to the state-of-the-art HSEs (PC, FF) and RC-S, RC-M and RC-L showed a denser cornified layer, suggesting improved stratification.

We then assessed the expression and localization of known markers for keratinocyte differentiation and skin tissue homeostasis [59]. Like normal skin, all HSEs showed Ki67 and keratin 14 (K14) expression in the basal layer similar to human skin in vivo [60]. Although radial constraint in HSEs resulted in an increased thickness of the epidermal equivalent (Fig. 2b), there was no significant difference in the number of Ki67⁺ keratinocytes (Fig. 4b) or in the relative *K14* gene expression (Fig. 4c) at the time point of fixation. Moreover, the junctional markers E-cadherin and its cytoplasmic partner β -catenin, as well as connexin 43 (CNX43) were correctly localized at cell-to-cell contacts (Fig. 4a) [61–65]. PC and RC-M and RC-L showed a better junctional organization. Of interest, only RC-L HSEs lacked CNX43 localization in the basal keratinocytes like in native skin.

We further evaluated the expression and localization of keratin 10 (K10), a marker for early keratinocyte differentiation, and of loricrin (Lor), a marker of late keratinocyte differentiation with an important role in epidermal barrier function [66–68]. Interestingly, radial constraint in HSEs influenced epidermal maturation. In particular, RC-M and RC-L showed stronger loricrin staining than state-of-the-art samples PC and FF (Fig. 4a), whereas the RC-S showed lowest expression of loricrin, indicating that the terminal differentiation process is dependent on the size of the culture insert. This observation is in line with the relative gene expression of *LOR* (Fig. 4d), confirming the observed significant differences in terminal differentiation of epidermal keratinocytes and epidermal stratification.

3.3.2. Static radial constraint in HSEs improves basement membrane continuity

As in native skin, all HSEs showed expression and correct localization of laminin 5 (Lam5), a major component of the basement membrane (Fig. 4a). In comparison to state-of-the-art samples (PC, FF) however, radially constrained samples showed a stronger expression of laminin 5. Moreover, RC-M and RC-L showed a more continuous layer of laminin 5-expressing cells than the remaining HSEs. The density of basal keratinocytes, i.e., number of basal keratinocytes per length (Fig. 4e), was similar in the state-of-the-art samples (PC, FF), whereas differences were observed across the RC samples. The density of keratinocytes increased with culture insert diameter.

Overall, the data suggest that the extent of radial constraint applied to the HSE influenced epidermal homeostasis and keratinocyte differentiation.

3.4. Computational simulation of strain, stress and principal directions in HSEs

A finite element study of all configurations was performed to investigate the spatial mechanical properties of the skin equivalents generated under the different conditions. The results of the computational analyses are shown in Fig. 5 for the final state of the process. Fig. 5a shows cross-sections of cultures with all configurations, with the magnitude of the radial component of the Cauchy stress tensor and the radial component of the Green-Lagrange strain tensor as well as the directions of the largest (red) and second largest (green) principal strain. In the PC sample, a mechanical restriction from the bottom surface is introduced [69]. Two areas can be distinguished in the sample. Close to the surface are large positive radial strains. They decrease quickly with increasing distance from the surface and change to compressive radial strains for the upper part of the sample. The radial component of the stress tensor remains in a low regime throughout the whole sample. The first principal strain (red) shows no preferred direction, while the second principal strain (green) is negative and aligned with the bottom in the center of the specimen. The FF sample, which is not restricted in its natural deformation, contracts homogeneously as expected [29,70]. High compression strains and low stresses are seen in the whole sample. Both principal strains show no preferred orientation. Possible inhomogeneities, which can occur during the production process, are not

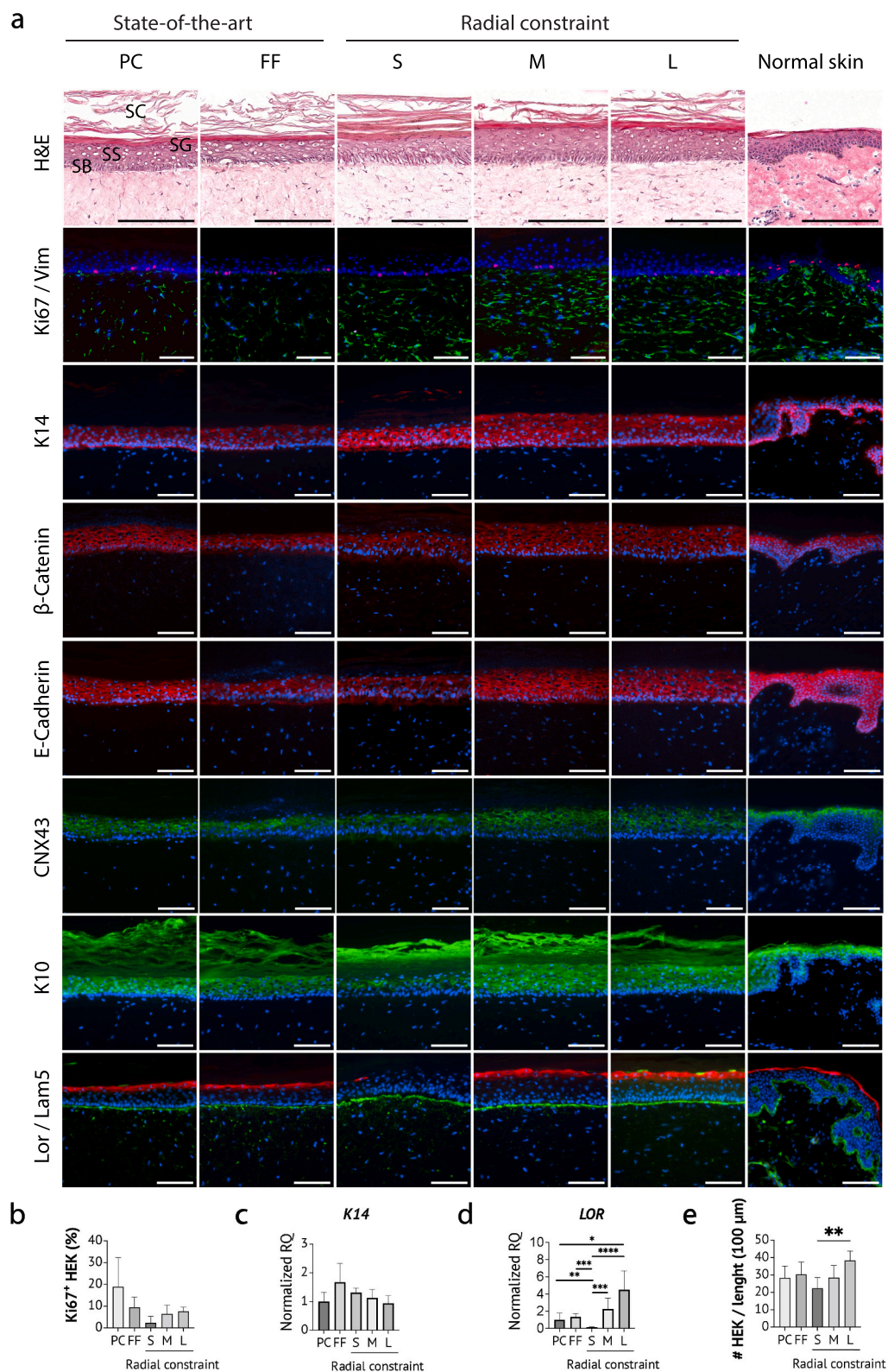


Fig. 4. Radial constraint improves keratinocyte differentiation, epidermal stratification, and basement membrane formation in HSEs.

(a) Representative H&E (uppermost panel) and immunofluorescence (IF) stainings of sections from HSEs and normal skin. *Stratum basale* (SB), *stratum spinosum* (SS), *stratum granulosum* (SG) and *stratum corneum* (SC). Samples were stained with antibodies against Ki67 (red), vimentin (Vim, green), keratin 14 (K14), β-catenin, E-cadherin, connexin 43 (Cnx43), keratin 10 (K10), loricrin (Lor) and laminin 5 (Lam5). Scale bars H&E: 200 μm, IF: 100 μm. **(b)** Percentage of Ki67⁺ basal keratinocytes. **(c-d)** qRT-PCR using RNA samples from isolated epidermal layers of HSEs for K14 and LOR. **(e)** Quantification of the number of basal keratinocytes per length (100 μm).

Graphs show mean ± SD. **P* < 0.05, ***P* < 0.01, ****P* < 0.001, *****P* < 0.0001 (one-way ANOVA with Turkey's multiple comparison test).

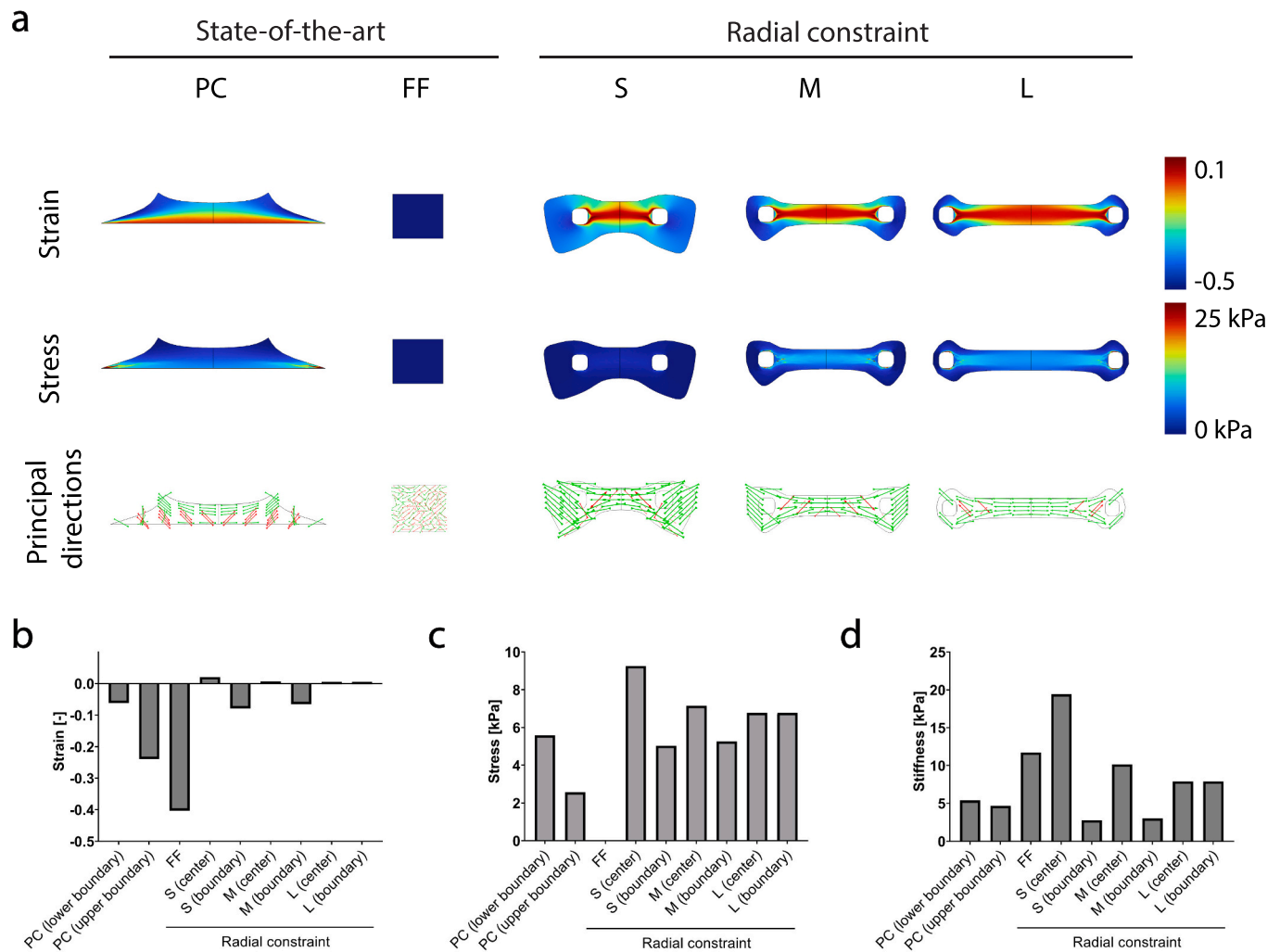


Fig. 5. FEM analysis of tissue deformation, principal strain direction and overall stiffness of collagen-based HSEs.

(a) Spatial distribution of magnitude of the radial component of the strain tensor, magnitude of the radial component of the stress tensor, and principal strain direction for all configurations. The radially constrained samples show a region of high radial strain and radial stress with a preferred radial direction of the largest (red) and second largest (green) principal strains.

(b) Average magnitude of the radial component of the strain tensor in the different regions,

(c) average magnitude of the radial component of the stress tensor in the region of interest and (d) average stiffness in radial direction in the region of interest.

captured by the homogenized finite element simulation [70]. In the RC samples, the boundaries of the sample in contact with the treated surface are fixed. The RC samples show a distinct difference in spatial mechanical properties compared to the state-of-the-art procedure. Especially, in the middle of the sample, the physical constraint of the insert strongly alters the stress and strain in the radial direction within the sample. All radially constrained samples show a positive radial strain with higher radial stress in the middle region. Further, the second largest principal strain is oriented in radial direction in the center region of the sample. The results of the average values for the magnitude of the radial component of the strain tensor, the magnitude of the radial component of the stress tensor, and the stiffness in radial direction in the regions of interest are shown in Fig. 5b–d. Two regions, a region in the center of the specimen (center region) and at the boundary (boundary region) are distinguished. The exact location of the regions is indicated in Supplementary Fig. 1. As expected, our analysis shows that the magnitude of the induced change of the component of the strain in radial direction differs only little between all three radially constrained samples. On the other hand, the diameter of the radial constraint influences the homogeneity of the induced mechanical stress and strain. The larger the insert, the more homogeneous the induced strain, which is visible in

Fig. 5a and Supplementary G. While for RC-S and RC-M samples a gradient from the center to the upper and lower boundary exists, the components of the stress and strain tensors in radial direction are constant for the RC-L sample and have a stronger influence on the boundary regions. In fact, the computational analysis shows that for RC-S almost no external mechanical stimulus is present at the epidermal surface (upper boundary).

4. Discussion

In this study, we took an approach to guide the tissue contraction of collagen-based HSEs to a defined final area by using 3D-printed culture inserts that enable the adhesion of the HSEs to its surface. We varied the diameter of the ring-shaped culture insert to apply different configurations of radial matrix constraint in bi-layered HSEs. We investigated the HSE's characteristics with respect to tissue structure and function and compared the resulting HSEs to state-of-the-art HSEs - unconstrained free-floating (FF) and planar constrained (PC) HSEs.

4.1. A simple and customizable tool for radial matrix constraint in skin engineering

In scaffold-based HSEs, the biomaterial that is used to generate the dermal layer is considered as the key component. Due to its abundance within native dermis and its high biocompatibility, collagen type I hydrogels are widely used as scaffold in HSEs [25]. However, such collagen-based hydrogels are susceptible to cell-mediated matrix contraction and often show poor mechanical stability [71,72]. This contraction mechanism causes irregular shape deformations that manifest in heterogeneous HSEs with respect to their morphological and mechanical properties [10,35,73]. HSEs are therefore often adhered to a surface, such as porous membranes of commercial transwells [29], porous silicon sheets [74] or polycaprolactone (PCL) nanofiber mesh or anchors [35,75], leading to a trapezoidal shape of the tissue. Such surface-adherent tissue constructs are thereby exposed to a planar constraint with the aim to allow epidermal seeding and to stabilize collagen-based constructs during tissue maturation.

For a more homogenous tissue construct, HSEs were adhered bi-axially to polymer anchors either via porosity [38] or O₂ plasma treatment of parylene C-coated polymer anchoring structures [26,76]. Both techniques allow stable fixation of the HSE to the anchoring structure. Similar to recent work, the culture system described here was designed with a circular shape [27,41]. However, in contrast to previous studies proposing radial constraint by pinching approaches, the culture system described here enables the HSE to adhere reliably to the culture insert via its hydrophilic surface (Supplementary F). Additionally, by changing the diameter of the ring-shaped culture insert, different magnitudes of area constraint can be achieved in the HSE. The HSE is mechanically stable during culture, thereby facilitating a user-friendly handling of HSEs. The system is further easily modifiable, produced at low-cost and fast by using additive manufacturing. Finally, most culture systems developed in recent years are sterilizable only by ethanol cleaning and UV light irradiation [26,35,39]. Our culture system is sterilizable by autoclaving at 120 °C, which enables sterile long-term culture of HSEs as well as the reuse of all parts.

4.2. Effects of various tissue constraints on HSE quality

Mechanical loading plays an important role in regulating cell phenotype as well as cell and ECM alignment [15,31,77]. Exposing skin constructs to physical constraint was shown to modulate the tissue's shape, homogeneity, and organization, as well as cellular functionality [15,26,27,35]. While various approaches have demonstrated this capability, only few studies have considered varying the magnitude of the applied loading conditions. These studies have shown that the observed effects in tissue organization and cellular functionality are dependent on the magnitude of the applied mechanical stimuli. These studies report the effect of varying the magnitude of uniaxial or biaxial adherence on dermal [38,40], epidermal [78] or bi-layered skin constructs [39]. In the following sections our results will be compared to these studies.

The HSEs established in this study can be classified by the type of physical restraint imposed experimentally. The free-floating (FF) and surface-restrained (PC) HSEs are state-of-the-art HSEs and served as comparison to the here developed radially constrained (RC) HSEs. In line with previous studies, all HSEs showed a characteristic contraction behavior and final appearance caused by the physical constraint applied [14,54]. FF- and PC-HSEs showed an overall heterogeneous cell and fiber orientation in the dermal equivalent [27] and a differentiated epidermal equivalent. The contraction of radially constrained HSEs was limited by the size of the culture insert and remained stable for the culturing phase. Dermal fibroblasts and ECM fibers in the dermal layer were oriented in the direction of the stress in the HSEs and comparable with other studies applying physical constraint to HSEs [15,26,76]. Cell and fiber alignment was thereby promoted by the increasing culture insert diameter

and resembled native skin more closely.

ECM turnover is part of healthy tissue maintenance where old proteins are degraded, and new proteins formed. It was shown that by applying additional external stress [39] or cyclic external stress to tissue constructs [41,79] ECM production and tissue strength increased. A recent study further showed that static physical constraint alone induced the production of ECM proteins such as different collagens, elastin and fibronectin, and simultaneously downregulated ECM degradation [27]. Our study shows additionally that ECM production depends on the geometry of the constraints and increases with increasing culture insert diameter.

Further, it was previously shown that application of external stress on bi-layered HSEs resulted in HSEs with a thicker and more differentiated epidermal equivalent [75,76]. Moreover, significantly greater expression levels of basement membrane components (i.e. laminin 5, collagen IV/VII) and development of a continuous basement membrane was reported [39,41,74]. Here, we show that applying static radial constraint in HSEs already significantly influenced epidermal thickness and epidermal maturation depending on the culture insert diameter. In particular, radial constraint samples RC-M and RC-L showed a significantly increased thickness of the epidermal equivalents and advanced keratinocyte organization and differentiation as well as a continuous basement membrane. In contrast, keratinocytes in the RC-S were not terminally differentiated. We hypothesize that applying static radial constraint not only improves HSE characteristics, but also promotes skin homeostasis through the activation of mechano-sensitive proteins in keratinocytes.

In healthy tissue, tissue remodeling and new matrix biosynthesis result in mechanical unloading, whereas persistent mechanical loading creates pathological conditions [80]. Since radial constraint in HSEs did not trigger pathological myofibroblast differentiation or increased fibroblast proliferation, and since no significant difference in the number of Ki67⁺ keratinocytes could be observed and the thickness of the living epidermal equivalent remained within the range of the thickness of normal human epidermis (75–100 µm) [81], we hypothesize that radially constraining HSEs can accelerate HSE production without inducing unphysiological cell behavior as for example seen in hyper-proliferative skin diseases [82]. However, to fully understand the role of mechano-sensitive molecules in the development of HSE characteristics, further studies are needed.

4.3. Finite element analysis and biological response

Our finite element analysis (FEA) showed that the geometrical characteristics of the boundary conditions associated with static radial constraint affected the maximum principal strain and stress direction, and the stiffness in the sample. As expected, we observed that the identified second principal direction from our FEA (Fig. 5a) is in line with the measured dermal cell and fiber directions (Fig. 3a–d). In addition, we identified a dependence between the mechanical stimulus at the epidermal surface (Fig. 5a–c) and the observed keratinocyte differentiation (Section 3.3.1). However, several limitations must be considered for the interpretation of our simulation results. As our proposed FEA model contains several simplifications (i.e., effect of the boundary condition, material model representation of spontaneous and active contraction), it does not account e.g., for the synthesis of new ECM proteins or the change of cellular functions. Hence, the stiffness simulated in our FEA analysis (Fig. 5d) shows an anti-correlation pattern with respect to the measured ECM production (Fig. 3e). Overall, the strain differences observed between the three RC samples in the FEA were larger than expected. However, explaining the differences between the RC samples solely based on the matrix stiffness might be an oversimplification of the mechanobiology. While there is a close dependence of fibroblast function on stiffness [83], also other factors such as the strain rate have been shown to be of importance [84]. In fact, fibroblast proliferation and skin growth were shown to be stimulated by cyclic

strain, thus underlying the importance of the deformation rate [41,84,85]. Deformation rates are the highest in our system during gel contraction in the first few days. A more detailed investigation of this timespan could provide valuable insight into the mechanobiology of dermal fibroblasts to understand the main cues for the biological differences shown in this study.

Finally, this analysis provides an FEA model predicting the differences in strains and stresses in the different configurations. A direct comparison of stresses and stiffnesses with native human skin would be of great interest for further research. Due to the complex deformation mechanism induced by the radial strain inserts, stresses and stiffnesses predicted by the finite element simulation should be interpreted with care. To enable a direct comparison of the biomechanical environment induced by the radial constraints with native human skin, thus requires a thorough experimental analysis of the nonlinear mechanical behavior of the hydrogel at complex deformations.

5. Conclusion

Mechanical cues in skin are essential for many biological processes in health and disease, and numerous in vivo conditions exhibit changes in the tissue's mechanical properties. Regulating mechanical factors in HSEs is therefore an important design consideration in tissue engineering of skin. In this study, we exposed collagen-based, bi-layered HSEs to different levels of radial constraints by varying the diameter of a ring-shaped culture insert. An increased diameter resulted in an increased alignment of dermal tissue and increased ECM production. Moreover, an increased diameter led to an increased thickness of the epidermal layer, advanced keratinocyte organization, increased epidermal differentiation, and a continuous basement membrane formation. These findings highlight the importance of considering the level of radial constraint as a design parameter in skin tissue engineering as it can be used to modulate the characteristics of HSEs.

Finally, it is known that uncontrolled cell-induced contraction is one of the major limitations of planar constrained HSEs and can result in high variability [73]. The reliable adherence of radially constrained HSEs to the herein developed culture insert can help to increase the reproducibility of in vitro HSEs by guiding tissue contraction to a defined final area. Furthermore, compared to state-of-the-art HSEs, using higher levels of radial constraint results in HSEs with increased dermal organization as well as enhanced terminal differentiation and junctional organization in the epidermal layer.

CRediT authorship contribution statement

Jessica Polak: Conceptualization, Methodology, Software, Validation, Formal analysis, Investigation, Data curation, Writing – original draft, Writing – review & editing, Visualization, Project administration. **David Sachs:** Methodology, Software, Formal analysis, Investigation, Writing – original draft, Writing – review & editing, Visualization. **Nino Scherrer:** Methodology, Software, Formal analysis, Investigation, Writing – original draft, Writing – review & editing, Visualization. **Adrian Süess:** Methodology, Validation, Investigation. **Huan Liu:** Methodology, Validation, Investigation. **Mitchell Levesque:** Resources, Writing – review & editing, Funding acquisition. **Sabine Werner:** Resources, Writing – review & editing, Supervision, Funding acquisition. **Edoardo Mazza:** Resources, Writing – review & editing, Supervision, Funding acquisition. **Gaetana Restivo:** Investigation, Writing – review & editing, Supervision. **Mirko Meboldt:** Conceptualization, Resources, Writing – review & editing, Supervision, Funding acquisition. **Costanza Giampietro:** Conceptualization, Investigation, Writing – review & editing, Supervision.

Declaration of competing interest

The authors declare that they have no known competing financial

interests or personal relationships that could have appeared to influence the work reported in this paper.

Data availability

Data will be made available on request.

Acknowledgments

We thank Michela Di Filippo, Mauro Esposito, Paul Hiebert and Theresa Rauschendorfer for helpful suggestions with qRT-PCR experiments and immunofluorescence, and Marcel Gort, Nikolaos Tachatos, Matthias Dupuch and Francesca Pramotton for their support with the 3D-printer, the parylene C coater and the plasma cleaner. Vartan Kurtcuoglu and Thomas Biedermann are acknowledged for providing valuable feedback during this project. Finally, the authors thank the Scientific Center for Optical and Electron Microscopy (ScopeM), ETH Zurich for support & assistance in this work. This work was supported by ETH Zurich (Open ETH Project SKINTEGRITY.CH) and core funding to M.M., E.M. and S.W., and by University of Zurich funding (SKINTEGRITY.CH collaborative research program) to M.L.

Appendix A. Supplementary data

Supplementary data to this article can be found online at <https://doi.org/10.1016/j.bioadv.2023.213702>.

References

- [1] S. MacNeil, Progress and opportunities for tissue-engineered skin, *Nature* 445 (7130) (2007), <https://doi.org/10.1038/nature05664>. Nature Publishing Group, pp. 874–880, Feb. 22.
- [2] H. Singh, et al., Nanoceria laden decellularized extracellular matrix-based curcumin releasing nanoemulgel system for full-thickness wound healing, *Biomaterials Advances* 137 (2022), 212806. Jun, <https://doi.org/10.1016/J.BIOADV.2022.212806>.
- [3] S. Guan, K. Zhang, L. Cui, J. Liang, J. Li, F. Guan, Injectable gelatin/oxidized dextran hydrogel loaded with apocynin for skin tissue regeneration, *Biomaterials Advances* 133 (2022), 112604. Feb, <https://doi.org/10.1016/J.MSEC.2021.112604>.
- [4] K. Pfisterer, L.E. Shaw, D. Symmank, W. Weninger, The extracellular matrix in skin inflammation and infection, *Front. Cell Dev. Biol.* 9 (2021) 1578. Jul, <https://doi.org/10.3389/FCCELL.2021.682414/BIBTEX>.
- [5] M.D. Malta, M.T. Cerqueira, A.P. Marques, Extracellular matrix in skin diseases: the road to new therapies, *J. Adv. Res.* (2022), <https://doi.org/10.1016/J.JARE.2022.11.008>. Dec.
- [6] N.N. Potekhaev, et al., Clinical medicine the role of extracellular matrix in skin wound healing, *J. Clin. Med.* (2021) 10, <https://doi.org/10.3390/jcm10245947>.
- [7] Y.K. Zhu, et al., Contraction of Fibroblast-Containing Collagen Gels: Initial Collagen Concentration Regulates the Degree of Contraction and Cell Survival, *Cell, Vitro Biology, Vitro*, 2001, pp. 10–16.
- [8] T.D. Allen, S.L. Schort, *The Contraction of Collagen Matrices by Dermal Fibroblasts* 219, 1983.
- [9] M.I. Patiño Vargas, et al., Viscoelastic properties of plasma-agarose hydrogels dictate favorable fibroblast responses for skin tissue engineering applications, *Biomaterials Advances* 139 (2022), 212967. Aug, <https://doi.org/10.1016/J.BIOADV.2022.212967>.
- [10] C. Lotz, F.F. Schmid, E. Oechsle, M.G. Monaghan, H. Walles, F. Groeber-Becker, Cross-linked collagen hydrogel matrix resisting contraction to facilitate full-thickness skin equivalents, *ACS Appl. Mater. Interfaces* 9 (24) (2017) 20417–20425, <https://doi.org/10.1021/acsami.7b04017>.
- [11] J. Xie, M. Bao, M.C. Bruekers, W.T.S. Huck, Collagen Gels with Different Fibrillar Microarchitectures Elicit Different Cellular Responses, 2017, <https://doi.org/10.1021/acsami.7b03883>.
- [12] R.A. Brown, M. Wiseman, C.B. Chuo, U. Cheema, S.N. Nazhat, Ultrarapid engineering of biomimetic materials and tissues: fabrication of nano- and microstructures by plastic compression, *Adv. Funct. Mater.* 15 (11) (2005) 1762–1770, <https://doi.org/10.1002/adfm.200500042>.
- [13] E. Braziliulis, et al., Modified plastic compression of collagen hydrogels provides an ideal matrix for clinically applicable skin substitutes, *Tissue Eng. Part C Methods* 18 (6) (2012) 464–474, <https://doi.org/10.1089/ten.tec.2011.0561>.
- [14] S. Nakagawa, P. Pawelek, F. Grinnell, Extracellular matrix organization modulates fibroblast growth and growth factor responsiveness, *Exp. Cell Res.* 182 (2) (1989) 572–582, [https://doi.org/10.1016/0014-4827\(89\)90260-7](https://doi.org/10.1016/0014-4827(89)90260-7).
- [15] G. Grenier, et al., Tissue reorganization in response to mechanical load increases functionality, *Tissue Eng.* 11 (1–2) (2005) 90–100, <https://doi.org/10.1089/ten.2005.11.90>.

- [16] M.H. Kural, K.L. Billiar, Regulating tension in three-dimensional culture environments, *Exp. Cell Res.* 319 (16) (2013) 2447–2459, <https://doi.org/10.1016/j.yexcr.2013.06.019>.
- [17] D.E. Discher, P. Janmey, Y.L. Wang, Tissue cells feel and respond to the stiffness of their substrate, *Science* (1979) 310 (5751) (2005) 1139–1143, <https://doi.org/10.1126/science.1116995>.
- [18] P. Gupta, et al., Substrate stiffness does affect the fate of human keratinocytes, *RSC Adv.* 6 (5) (2016) 3539–3551, <https://doi.org/10.1039/c5ra19947f>.
- [19] F.N. Kenny, et al., Tissue stiffening promotes keratinocyte proliferation through activation of epidermal growth factor signaling, *J. Cell Sci.* 131 (10) (2018), <https://doi.org/10.1242/jcs.215780>.
- [20] G.H. Altman, et al., Cell differentiation by mechanical stress, *The FASEB journal : official publication of the Federation of American Societies for Experimental Biology* 16 (2) (2002) 270–272, <https://doi.org/10.1096/fj.01-0656fje>.
- [21] A.J. Engler, S. Sen, H.L. Sweeney, D.E. Discher, Matrix elasticity directs stem cell lineage specification, *Cell* 126 (4) (2006) 677–689, <https://doi.org/10.1016/j.cell.2006.06.044>.
- [22] J.H. Wang, B. Li, Open access review mechanics rules cell biology, *Therapy & Technology* 2 (2010) 16.
- [23] C.K. Hsu, H.H. Lin, H.L.C. Harn, M.W. Hughes, M.J. Tang, C.C. Yang, Mechanical forces in skin disorders, *J. Dermatol. Sci.* 90 (3) (2018) 232–240, <https://doi.org/10.1016/j.jdermsci.2018.03.004>.
- [24] J.D. Humphrey, E.R. Dufresne, M.A. Schwartz, Mechanotransduction and extracellular matrix homeostasis, *Nat. Rev. Mol. Cell Biol.* 15 (12) (2014) 802–812, <https://doi.org/10.1038/nrm3896>.
- [25] F.A. Auger, M. Rouabhi, F. Goulet, F. Berthod, V. Moulin, L. Germain, Tissue-engineered human skin substitutes developed from collagen-populated hydrated gels: clinical and fundamental applications, *Med. Biol. Eng. Comput.* 36 (6) (1998) 801–812, <https://doi.org/10.1007/BF02518887>.
- [26] N. Mori, Y. Morimoto, S. Takeuchi, Skin integrated with perfusable vascular channels on a chip, *Biomaterials* 116 (2017) 48–56, <https://doi.org/10.1016/j.biomaterials.2016.11.031>.
- [27] S. Kimura, et al., Tissue-scale tensional homeostasis in skin regulates structure and physiological function, *Commun Biol* 3 (1) (2020) 1–14, <https://doi.org/10.1038/s42003-020-01365-7>.
- [28] T. Elsdale, J. Bard, Collagen studies substrata for cell cultures collection and solubilization procedures for counting petri dish cultures labeled preparation of hydrated collagen lattices downloaded from jcb .rnpres .org on May 30, 2010 superficial characteristics of HC, *J. Cell Biol.* (1972) 626–637.
- [29] E. Bell, B. Ivarsson, C. Merrill, Production of a tissue-like structure by contraction of collagen lattices by human fibroblasts of different proliferative potential in vitro, *Proc. Natl. Acad. Sci. U. S. A.* 76 (3) (1979) 1274–1278, <https://doi.org/10.1073/pnas.76.3.1274>.
- [30] F. Grinnell, C.H. Ho, Y.C. Lin, G. Skuta, Differences in the regulation of fibroblast contraction of floating versus stressed collagen matrices, *J. Biol. Chem.* 274 (2) (1999) 918–923, <https://doi.org/10.1074/jbc.274.2.918>.
- [31] F. Grinnell, Fibroblast biology in three-dimensional collagen matrices, *Trends Cell Biol.* 13 (5) (2003) 264–269, [https://doi.org/10.1016/S0962-8924\(03\)00057-6](https://doi.org/10.1016/S0962-8924(03)00057-6).
- [32] F. Grinnell, W.M. Petroll, Cell motility and mechanics in three-dimensional collagen matrices, *Annu. Rev. Cell Dev. Biol.* 26 (2010) 335–361, <https://doi.org/10.1146/annurev.cellbio.042308.113318>.
- [33] M.B. Vaughan, G. Xu, T.L. Morris, P. Kshetri, X. Jing, Predictable fibroblast tension generation by measuring compaction of anchored collagen matrices using microscopy and optical coherence tomography collagen matrices using microscopy and optical coherence tomography, *Cell Adh. Migr.* 13 (1) (2019) 302–313, <https://doi.org/10.1080/109336918.2019.1644855>.
- [34] M. Miron-Mendoza, J. Seemann, F. Grinnell, Diacylglycerol is required for the formation of COPI vesicles in the Golgi-to-ER transport pathway, *Mol. Biol. Cell* 18 (May) (2007) 3250–3263, <https://doi.org/10.1091/mbc.E07>.
- [35] B.S. Kim, J.S. Lee, G. Gao, D.W. Cho, Direct 3D cell-printing of human skin with functional transwell system, *Biofabrication* 9 (2) (2017), <https://doi.org/10.1088/1758-5090/aa71c8>.
- [36] J. Fohlen, T. Yamashita, P. Kollmannsberger, Shaping tissues by balancing active forces and geometric constraints, *J. Phys. D Appl. Phys.* 49 (5) (2015), <https://doi.org/10.1088/0022-3727/49/5/053001>.
- [37] M.J. Eichler, M.A. Carlson, Modeling dermal granulation tissue with the linear fibroblast-populated collagen matrix: a comparison with the round matrix model, *J. Dermatol. Sci.* 41 (2) (2006) 97–108, <https://doi.org/10.1016/j.jdermsci.2005.09.002>.
- [38] J. John, A. Throm Quinlan, C. Silvestri, K. Billiar, Boundary stiffness regulates fibroblast behavior in collagen gels, *Ann. Biomed. Eng.* 38 (3) (2010) 658–673, <https://doi.org/10.1007/s10439-009-9856-1>.
- [39] H.M. Powell, K.L. McFarland, D.L. Butler, D.M. Supp, S.T. Boyce, Uniaxial strain regulates morphogenesis, gene expression, and tissue strength in engineered skin, *Tissue Eng. Part A* 16 (3) (2010) 1083–1092, <https://doi.org/10.1089/ten.tea.2009.0542>.
- [40] C.A. Derderian, et al., Mechanical strain alters gene expression in an in vitro model of hypertrophic scarring, *Ann. Plast. Surg.* 55 (1) (2005) 69–75, <https://doi.org/10.1097/01.sap.0000168160.86221.e9>.
- [41] A. Wahlsten, et al., Mechanical stimulation induces rapid fibroblast proliferation and accelerates the early maturation of human skin substitutes, *Biomaterials* 273 (2021), 120779, <https://doi.org/10.1016/j.biomaterials.2021.120779>.
- [42] A. Saltari, et al., CD271 Down-regulation promotes melanoma progression and invasion in three-dimensional models and in zebrafish, *Journal of Investigative Dermatology* 136 (10) (2016) 2049–2058, <https://doi.org/10.1016/j.jid.2016.05.116>.
- [43] W. Ehlers, N. Karajan, B. Markert, An extended biphasic model for charged hydrated tissues with application to the intervertebral disc, *Biomech. Model. Mechanobiol.* 8 (3) (2009) 233–251, <https://doi.org/10.1007/s10237-008-0129-y>.
- [44] A. Stracuzzi, E. Mazza, A.E. Ehret, Chemomechanical models for soft tissues based on the reconciliation of porous media and swelling polymer theories, *ZAMM Zeitschrift für Angewandte Mathematik und Mechanik* 98 (12) (2018) 2135–2154, <https://doi.org/10.1002/zamm.201700344>.
- [45] G. Himpel, E. Kuhl, A. Menzel, P. Steinmann, Computational modelling of isotropic multiplicative growth, *Computer Modeling in Engineering Science* 8 (2005) 119–134, <https://doi.org/10.3970/cmesci.2005.008.119>.
- [46] W. Ehlers, N. Karajan, B. Markert, An extended biphasic model for charged hydrated tissues with application to the intervertebral disc, *Biomech. Model. Mechanobiol.* 8 (3) (2009) 233–251, Jun, <https://doi.org/10.1007/s10237-008-0129-y>.
- [47] A. Stracuzzi, E. Mazza, A.E. Ehret, Chemomechanical models for soft tissues based on the reconciliation of porous media and swelling polymer theories, *ZAMM Zeitschrift für Angewandte Mathematik und Mechanik* (2018), <https://doi.org/10.1002/zamm.201700344>.
- [48] W.R. Legant, J.S. Miller, B.L. Blakely, D.M. Cohen, G.M. Genin, C.S. Chen, Measurement of mechanical tractions exerted by cells in three-dimensional matrices, *Nature Methods* 2010 7:12 7 (12) (Nov. 2010) 969–971, <https://doi.org/10.1038/nmeth.1531>.
- [49] D. Sachs, A. Wahlsten, S. Kozerke, G. Restivo, E. Mazza, A biphasic multilayer computational model of human skin, *Biomech. Model. Mechanobiol.* 20 (3) (2021) 969–982, Jun, <https://doi.org/10.1007/s10237-021-01424-W/FIGURES/14>.
- [50] D. Sachs, A. Wahlsten, S. Kozerke, G. Restivo, E. Mazza, A biphasic multilayer computational model of human skin, *Biomech. Model. Mechanobiol.* 20 (3) (2021) 969–982, <https://doi.org/10.1007/s10237-021-01424-w>.
- [51] A. Wahlsten, M. Pensalfini, A. Stracuzzi, G. Restivo, R. Hopf, E. Mazza, On the compressibility and poroelasticity of human and murine skin, *Biomechanics and Modeling in Mechanobiology* 2019 18:4 18 (4) (Feb. 2019) 1079–1093, <https://doi.org/10.1007/s10237-019-01129-1>.
- [52] M. Pensalfini, et al., Factors affecting the mechanical behavior of collagen hydrogels for skin tissue engineering, *J. Mech. Behav. Biomed. Mater.* 69 (2017) 85–97, May, <https://doi.org/10.1016/j.jmbbm.2016.12.004>.
- [53] P. Bankhead, et al., QuPath: open source software for digital pathology image analysis, *Sci. Rep.* 7 (1) (2017), <https://doi.org/10.1038/s41598-017-17204-5>.
- [54] J.F. Eichinger, L.J. Haeusel, D. Paukner, R.C. Aydin, J.D. Humphrey, C.J. Cyron, Mechanical homeostasis in tissue equivalents: a review, *Biomech. Model. Mechanobiol.* no. 1987 (2021), <https://doi.org/10.1007/s10237-021-01433-9>.
- [55] L. Weber, E. Kirsch, P. Muller, T. Krieg, Collagen type distribution and macromolecular organization of connective tissue in different layers of human skin, *J. Invest. Dermatol.* 82 (2) (1984) 156–160, <https://doi.org/10.1111/1523-1747.ep12259720>.
- [56] W.N. Meigel, S. Gay, L. Weber, Dermal architecture and collagen type distribution, *Arch. Dermatol. Res.* 259 (1) (1977) 1–10, <https://doi.org/10.1007/BF00562732>.
- [57] S. Bancelin, et al., Ex vivo multiscale quantitation of skin biomechanics in wild-type and genetically-modified mice using multiphoton microscopy, *Sci. Rep.* 5 (December) (2015) 1–14, <https://doi.org/10.1038/srep17635>.
- [58] I.A.N.A. Brown, A Scanning Electron Microscope Study of the Effects of Uniaxial Tension on Human Skin, 1973, pp. 383–394.
- [59] L. Pontiggia, et al., Markers to evaluate the quality and self-renewing potential of engineered human skin substitutes in vitro and after transplantation, *Journal of Investigative Dermatology* 129 (2) (2009) 480–490, <https://doi.org/10.1038/jid.2008.254>.
- [60] T. Baltazar, et al., Three dimensional bioprinting of a vascularized and perfusable skin graft using human keratinocytes, fibroblasts, pericytes, and endothelial cells, *Tissue Eng. Part A* 26 (5–6) (2020) 227–238, <https://doi.org/10.1089/ten.tea.2019.0201>.
- [61] X.F.E.I. Zhang, X. Cui, Connexin 43 : Key Roles in the Skin (Review) vol. 1, no. 16, 2017, pp. 605–611, <https://doi.org/10.3892/br.2017.903>.
- [62] P. Young, et al., E-cadherin Controls Adherens Junctions in the Epidermis and the Renewal of Hair Follicles vol. 22, no. 21, 2003, pp. 5723–5733.
- [63] J. Huelsken, R. Vogel, B. Erdmann, G. Cotsarelis, W. Birchmeier, β -Catenin Controls Hair Follicle Morphogenesis and Stem Cell Differentiation in the Skin 105, 2001, pp. 533–545.
- [64] D. Stamenović, M.L. Smith, Tensional homeostasis at different length scales, *Soft Matter* 16 (30) (2020) 6946–6963, <https://doi.org/10.1039/d0sm00763c>.
- [65] L.C. Biggs, C.S. Kim, Y.A. Miroshnikova, S.A. Wickström, Mechanical forces in the skin: roles in tissue architecture, stability, and function, *Journal of Investigative Dermatology* 140 (2) (2020) 284–290, <https://doi.org/10.1016/j.jid.2019.06.137>.
- [66] Y. Ishitsuka, *Loricrin: Past, Present, and Future* 12, no. Li, 2020.
- [67] F. Wang, A. Ziemann, P.A. Coulombe, *Skin Keratins* 1st ed, 568, Elsevier Inc., 2016, <https://doi.org/10.1016/bs.mie.2015.09.032>.
- [68] S. Nithya, T. Radhika, N. Jeddy, *Loricrin – An Overview* vol. 19, no. 1, 2015, pp. 64–68, <https://doi.org/10.4103/0973-029X.157204>.
- [69] F. Grinnell, Fibroblasts, myofibroblasts, and wound contraction, *Journal of Cell Biology* 124 (1994) 401–404, <https://doi.org/10.1083/jcb.124.4.401>, no. 4. Rockefeller University Press.
- [70] D.D. Simon, C.O. Horgan, J.D. Humphrey, Mechanical restrictions on biological responses by adherent cells within collagen gels, *J. Mech. Behav. Biomed. Mater.* 14 (2012) 216–226, <https://doi.org/10.1016/j.jmbbm.2012.05.009>.
- [71] P. Gangatirak, S. Paquet-Fifield, A. Li, R. Rossi, P. Kaur, Establishment of 3D organotypic cultures using human neonatal epidermal cells, *Nat. Protoc.* 2 (1) (2007) 178–186, <https://doi.org/10.1038/nprot.2006.448>.

- [72] H.J. Stark, et al., Epidermal homeostasis in long-term scaffold-enforced skin equivalents, *J. Investig. Dermatol. Symp. Proc.* (2006) 93–105, <https://doi.org/10.1038/sj.jidsymp.5650015>, Sep.
- [73] C.A. Harrison, S. MacNeil, The mechanism of skin graft contraction: an update on current research and potential future therapies, *Burns* 34 (2) (2008) 153–163, <https://doi.org/10.1016/j.burns.2007.08.011>.
- [74] E. Tokuyama, Y. Nagai, K. Takahashi, Y. Kimata, K. Naruse, Mechanical stretch on human skin equivalents increases the epidermal thickness and develops the basement membrane, *PLoS One* 10 (11) (2015) 1–12, <https://doi.org/10.1371/journal.pone.0141989>.
- [75] M.H. Jung, S.M. Jung, H.S. Shin, Co-stimulation of HaCaT keratinization with mechanical stress and air-exposure using a novel 3D culture device, *Sci. Rep.* 6 (May) (2016) 1–7, <https://doi.org/10.1038/srep33889>.
- [76] N. Mori, Y. Morimoto, S. Takeuchi, Perfusable and stretchable 3D culture system for skin-equivalent, *Biofabrication* 11 (1) (2019), <https://doi.org/10.1088/1758-5090/aaed12>, Jan.
- [77] M. Eastwood, V.C. Muder, D.A. McGrouther, R.A. Brown, Effect of precise mechanical loading on fibroblast populated collagen lattices: morphological changes, *Cell Motil. Cytoskeleton* 40 (1) (1998) 13–21, [https://doi.org/10.1002/\(SICI\)1097-0169\(1998\)40:1<13::AID-CM2>3.0.CO;2-G](https://doi.org/10.1002/(SICI)1097-0169(1998)40:1<13::AID-CM2>3.0.CO;2-G).
- [78] S. Yano, M. Komine, M. Fujimoto, H. Okochi, K. Tamaki, Mechanical stretching in vitro regulates signal transduction pathways and cellular proliferation in human epidermal keratinocytes, *Journal of Investigative Dermatology* 122 (3) (2004) 783–790, <https://doi.org/10.1111/j.0022-202X.2004.22328.x>.
- [79] A. Petersen, P. Joly, C. Bergmann, G. Korus, G.N. Duda, The impact of substrate stiffness and mechanical loading on fibroblast-induced scaffold remodeling, *Tissue Eng. Part A* 18 (17–18) (2012) 1804–1817, <https://doi.org/10.1089/ten.tea.2011.0514>.
- [80] J.J. Tomasek, G. Gabbiani, B. Hinz, C. Chaponnier, R.A. Brown, Myofibroblasts and mechano: regulation of connective tissue remodelling, *Nat. Rev. Mol. Cell Biol.* 3 (5) (2002) 349–363, <https://doi.org/10.1038/nrm809>.
- [81] J. Sandby-Møller, T. Poulsen, H.C. Wulf, Epidermal thickness at different body sites: relationship to age, gender, pigmentation, blood content, skin type and smoking habits, *Acta Derm. Venereol.* 83 (6) (2003) 410–413, <https://doi.org/10.1080/00015550310015419>.
- [82] H. Niehues, et al., Identification of keratinocyte mitogens: implications for Hyperproliferation in psoriasis and atopic dermatitis, *JID Innov* 2 (1) (2022), 100066, <https://doi.org/10.1016/j.xjidi.2021.100066>.
- [83] E. Hadjipanayi, V. Muder, R.A. Brown, Close dependence of fibroblast proliferation on collagen scaffold matrix stiffness, *J. Tissue Eng. Regen. Med.* 3 (2) (2009) 77–84, <https://doi.org/10.1002/term.136>.
- [84] M.S. Chin, et al., In vivo acceleration of skin growth using a servo-controlled stretching device, *Tissue Eng. Part C Methods* 16 (3) (2010) 397–405, <https://doi.org/10.1089/ten.tec.2009.0185>.
- [85] K.S. Park, E.G. Lee, Y. Son, Uniaxial cyclic strain stimulates cell proliferation and secretion of interleukin-6 and vascular endothelial growth factor of human dermal fibroblasts seeded on chitosan scaffolds, *J. Biomed. Mater. Res. A* 102 (7) (2014) 2268–2276, <https://doi.org/10.1002/jbm.a.34881>.